Cellular and Molecular Life Sciences (2025) 82:138
https://doi.org/10.1007/s00018-025-05666-0

Cellular and Molecular Life Sciences

ORIGINAL ARTICLE

PRDM16 suppresses pyroptosis to attenuate the progression of AKI caused by rhabdomyolysis via upregulation of USP10

Bocheng Han[1,2] · Qiang Zheng[2,4] · Huiling Li[3] · Yongjun Wang[1] · Dongshan Zhang[2,5]

Received: 22 February 2025 / Revised: 15 March 2025 / Accepted: 17 March 2025

Abstract

Previous studies have indicated that PRDM16 suppresses apoptosis and ferroptosis, thereby mitigating the development of AKI triggered by ischemia, cisplatin, and sepsis. Nevertheless, the exact function and control mechanisms of PRDM16 in rhabdomyolysis-induced AKI are not fully understood. In this investigation, PRDM16 was found to inhibit ferrous myoglobin-induced pyroptosis in Boston University mouse proximal tubule (BUMPT) cells. At the molecular level, PRDM16 binds to the USP10 promoter, enhancing its expression and subsequently inhibiting the NLRP3-Caspase1-GSDMD and Caspase3-GSDME pathways. Rhabdomyolysis-induced AKI was alleviated in PRDM16 KI mice, whereas PRDM16 KO exacerbated the condition. Furthermore, PNPs-encapsulated formononetin significantly attenuated the progression of rhabdomyolysis-induced AKI. In conclusion, PRDM16 suppresses pyroptosis and ameliorates rhabdomyolysis-induced AKI by regulating the USP10/NLRP3-Caspase1-GSDMD and Caspase3-GSDME pathways. PNPs-encapsulated formononetin emerges as a promising therapeutic strategy.

Graphical Abstract

PRDM16 binds to the USP10 promoter, enhances its expression, and subsequently suppresses pyroptosis, thereby attenuating the progression of AKI caused by rhabdomyolysis.

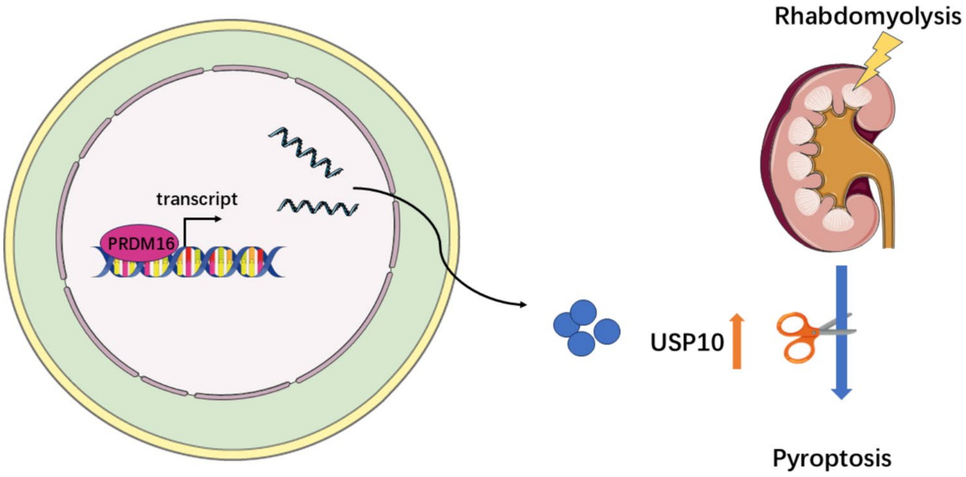

Keywords Acute kidney injury · Platelet membrane · Pyroptosis · Nano-based drug delivery · USP10 · PRDM16

Abbreviations

AKI	Acute kidney injury
BUMPT	Boston University mouse proximal tubule
BUN	Blood urea nitrogen
DOX	Doxycycline
NLRP3	NOD- LRR- and pyrin domain-containing protein 3
NTA	Nanoparticle tracking analyzer
PRDM16	PRD1-BF1-RIZ1 Homologous domain-containing protein 16

Extended author information available on the last page of the article

PNPs	Platelet membrane-coated nanoparticles
RM-AKI	Rhabdomyolysis-induced acute kidney injury
USP10	Ubiquitin Specific Peptidase 10

Introduction

Rhabdomyolysis (RM), characterized by the destruction of skeletal muscle fibers, leads to the release of myoglobin into the bloodstream. This myoglobin is filtered by the glomerulus, where it reaches the proximal tubules, causing damage and inducing acute kidney injury (AKI) [1–3]. RM is typically caused by crush injuries, medications, or intense physical exertion, with approximately 50% of cases resulting in AKI [4]. Furthermore, some AKI cases progress to chronic kidney disease (CKD) [5], leading to higher morbidity, mortality, and medical costs associated with RM [6, 7]. To date, effective therapies to prevent the progression of RM-induced AKI, apart from dialysis, remain unavailable. Thus, understanding the underlying mechanisms of renal tubular injury and identifying novel therapeutic strategies to alleviate RM-induced AKI is crucial.

RM induces extensive proximal tubule cell death, with apoptosis being the primary mode of cell death. Recent studies have highlighted that ferroptosis and pyroptosis also contribute to AKI progression [8–14]. Nevertheless, the control pathways governing pyroptosis in RM-induced AKI remain predominantly unexplored. Previous research demonstrated that PRDM16 mitigates AKI induced by LPS, cisplatin, and ischemia by inhibiting ferroptosis and apoptosis [15, 16]. However, it remains to be determined whether PRDM16 can also inhibit pyroptosis to attenuate RM-induced AKI.

This study reports for the first time that PRDM16 functions as an inhibitor of pyroptosis in tubular cells induced by myoglobin and glycerol in both in vitro and in vivo models. At the molecular level, PRDM16 suppresses pyroptosis through the upregulation of USP10, which in turn inhibits the ROS-NLRP3-Caspase1-GSDMD and Caspase3-GSDME pathways, along with LDH, IL-1β, and IL-18 level. Moreover, PNPs-encapsulated formononetin significantly ameliorates the progression of RM-induced AKI, presenting a promising novel therapeutic approach.

Material and methods

Antibodies and reagents

The primary antibodies employed in this investigation consisted of: anti-PRDM16 (Cat# PA5-20872, Thermo Scientific), anti-β-actin (Cat# 66009-1-Ig, Proteintech), anti-USP10 (Cat# 19374-1-AP, Proteintech), anti-GSDME (Cat# ab215191, Abcam), anti-HA-Tag (Cat# 3724, CST), anti-Caspase-3 (Cat# 9662, CST), anti-Cleaved Caspase-3 (Cat# 9664, CST), anti-NLRP3 (Cat# T55651, Abmart), anti-GSDMD (Cat# 20770-1-AP, Proteintech), anti-Cleaved GSDMD (Cat# 10137, CST), anti-Cleaved Caspase-1 (Cat# 89332, CST), anti-CD62p (Cat# bs-0561R, Bioss). Secondary antibodies were procured from Affinity (Wuhan, China). An enhanced chemiluminescence assay kit (Cat# 180–5001, Tanon, Shanghai, China) was used for protein band detection. USP10 plasmid, PRDM16 shRNA, and USP10 shRNA were procured from Genechem (Shanghai, China). Doxycycline (DOX) was sourced from Shenzhen Institutes of Advanced Technology, Chinese Academy of Sciences. PLGA 50:50 (Cat# MB5649-1, Meilunbio) and formononetin were obtained from the Guangzhou Institute of Biomedicine and Health, Guangzhou, China.

Cell culture and treatments

The BUMPT cell line (Boston University mouse proximal tubular cells) was kept in Dulbecco's modified Eagle's medium (DMEM) supplemented with 10% fetal bovine serum, 0.5% penicillin, and streptomycin, and incubated in a 5% CO_2 atmosphere at 37 °C [17]. A DOX-induced HA-PRDM16 stable cell line was established following our previous protocol [18], using 500 ng/ml of doxycycline. Cells underwent transfection with PRDM16 shRNA (100 nM), USP10 shRNA (100 nM), USP10 plasmid (1 µg/ml), or scramble shRNA and empty plasmid utilizing Lipofectamine™ 2000 (Thermo Scientific, USA). The cellular model of RM-AKI was established as described previously [10, 19], where BUMPT cells were incubated with 200 mM ferrous myoglobin for 24 h. Cells were pretreated with Disulfiram (0.5 µM, HY-B0240, MCE, China) and Z-DEVD-FMK (100 µM, HY-12466, MCE, China) for 2 h prior to experimentation.

Animal model of rhabdomyolysis-induced AKI

All animal experiments were executed per the protocols set by the Animal Care Ethics Committee of the Second Xiangya Hospital of Central South University (No. 2018065). Steps were taken to reduce animal usage and minimize their distress. Eight-to-ten-week-old male C57BL/6J mice were procured from SJA Laboratory Animal Ltd (Changsha, China) and kept in the Animal Experimental Center of the Second Xiangya Hospital. Mice were anesthetized using sodium pentobarbital. The proximal tubule-specific PRDM16-knockout (PT-PRDM16-KO) and PRDM16 knock-in (PT-PRDM16-KI) mice were generated as previously described [18]. These mice were kept under regulated conditions with alternating 12-h light/dark periods and unrestricted food and water availability. To induce RM-induced acute kidney injury (RM-AKI), mice received a 7.5 mL/kg injection of 50% glycerol diluted in sterile water into the skeletal muscles of the hind limbs bilaterally, as previously reported [20]. The control group received an equivalent amount of normal saline. Mice were sacrificed at 12- and 24-h post-injection, and kidney tissue and blood samples were collected for analysis. PNPs encapsulated with 20 mg/kg formononetin were administered via tail vein injection 30 min following RM-AKI induction.

Assessment of cell viability and LDH

Cells were placed at 5000 cells/100 µL in 96-well plates. After treatment, cell viability and LDH levels were assessed utilizing the Viability/Cytotoxicity Multiplex Assay Kit (CK17, Dojindo, Japan) per the supplier's protocol. Absorbance was ascertained utilizing a Spark® Multi-function Microplate Detector (TECAN, Switzerland).

Flow cytometry detection of ROS

Cellular reactive oxygen species (ROS) levels were ascertained utilizing the Reactive Oxygen Species Assay Kit (MA0219, Meilunbio, China). The fluorescence intensity change of the DCFH-DA (2,7-Dichlorod-hydrofluorescein diacetate) probe was utilized to quantify intracellular ROS levels. Fluorescence intensity was measured by flow cytometry (Cytek, USA) according to the kit protocol.

Relative quantitative real-time PCR (RT−qPCR)

Total RNA was procured from the renal cortex or BUMPT cells utilizing RNAiso Plus reagent (Cat# 9108, Takara, Japan). cDNA was generated utilizing the Evo M-MLV Reverse Transcription Kit (Cat# AG11705, Accurate Biology, China). RT-PCR quantification was executed utilizing SYBR Green Pro Taq HS reagent (Cat# AG11702, Accurate Biology, China) and a LightCycler 96 system (Roche). Relative quantification was calculated utilizing the ΔΔCT technique. The primer sequences employed for RT-qPCR were as follows: (Mouse) β-actin: forward Primer 5′-GGCTGTATTCCCCTCCATCG-3′, reverse Primer 5′-CCAGTTGGTAACAATGCCATGT-3′; (Mouse) PRDM16: forward Primer 5′-CAGCACCTCCAGCGTCACATC-3′, reverse Primer 5′-GCGAAGGTCTTGCCACAGTCAG-3′; (Mouse) USP10: forward Primer 5′- AACCCACAGTATATCTTTGGCG-3′, reverse Primer 5′-CCCTCACTAGGTTCGATGACTTC-3′.

Western blotting (WB)

Protein extracts from mouse renal cortex or BUMPT cells were procured utilizing RIPA buffer comprising protease inhibitors. Equal amounts of protein samples underwent SDS-PAGE fractionation and were subsequently blotted onto Polyvinylidene difluoride (PVDF) membranes. The membranes underwent blocking with 5% skim milk and subsequent overnight exposure to primary antibodies at 4 °C. Following PBST washes, the membranes were exposed to horseradish peroxidase (HRP)-linked secondary antibodies. Protein band detection was accomplished utilizing NcmECL Ultra (Cat# P10200, NCM Biotech, China). WB images were captured using a gel documentation system (Tanon, China), and band density quantification was performed using ImageJ (version 1.54 g).

Immunofluorescence staining

Immunofluorescence staining of BUMPT cells was performed as per the manufacturer's instructions (Cat# P0183, Beyotime, China). Cells grown on coverslips were incubated with PRDM16 antibody (1:500 dilution) overnight at 4 °C, succeeded by exposure to the secondary antibody for 1 h at ambient temperature. Cell nuclei underwent DAPI staining for 3–5 min. Immunofluorescence images were procured utilizing an Eclipse Ti laser scanning confocal microscope (Nikon, Japan), and relative fluorescence intensity was quantified using ImageJ software (version 1.54 g).

ChIP analysis

Chromatin immunoprecipitation sequencing (ChIP-seq) data utilized in this investigation were obtained from two sources. The first part of the data was from our previous study, which involved ChIP-seq analysis of a DOX-induced HA-PRDM16 stable cell line [18]. The second part was procured from the Gene Expression Omnibus (GEO) database, with the access number GSE131487. This dataset includes ChIP-seq data from the intestine tissue of control and PRDM16-knockout mice [21]. All ChIP-seq data were depicted through Integrative Genomics Viewer (IGV, version 2.18.4) [22]. The binding sites and motifs of PRDM16 in the USP10 promoter region were predicted using the online tool MoloTool [23]. ChIP PCR and ChIP qPCR experiments were performed per the protocol outlined in the ChIP Assay Kit (Cat# P2078, Beyotime, China). The primers used in these experiments were designed using NCBI's online tool (primer blast), and the target amplified fragments contain the predicted binding sites. The primers are as follows: P1 Forward primer 5′-TCCCCAATGCCAGGTAAAACA-3′, Reverse primer 5′-TCCCCAATGCCAGGTAAAACA-3′; P2 Forward primer 5′-GTACTAGGGAAGTAGGGGCGG-3′, Reverse primer 5′-TGTAAAGCCCCAGCTGTCCTG-3′.

Measurement of IL-18, IL-1β, BUN, and creatinine

ELISA experiments for the detection of cytokines were performed using the Mouse IL-1β ELISA Kit (Cat# PI301, Beyotime, China) and Mouse IL-18 ELISA Kit (Cat# PI553, Beyotime, China). BUN and creatinine levels were measured using the Urea-Nitrogen-Content Assay Kit (Beijing Boxbio Science & Technology) and Creatinine (Cr) Assay Kit (sarcosine oxidase) (Nanjing-Jiancheng Bioengineering Institute, Nanjing, China), respectively.

HE, TUNEL, DHE staining, immunohistochemical staining, and qualification

Histological damage was assessed using Hematoxylin and eosin (H&E) staining. Tubular damage [24] was scored utilizing the percentage of injured tubules, with the following grading scale: 0% (0); < 25% (1); 25%–50% (2); 50%–75% (3); and > 75% (4). Four fields chosen at random were evaluated, and their mean score was determined. TUNEL staining was executed utilizing the TUNEL kit (Cat # G1502, Servicebio, China), and the number of TUNEL-positive cells was counted in 10–20 randomly selected fields per tissue section. Dihydroethidium (DHE) staining was employed to examine ROS levels in kidney tissue. Renal cryosections were incubated with DHE solution (Cat #D7008, Sigma Aldrich, Germany) for 1 h, washed, and examined under fluorescence microscopy. The DHE fluorescence intensity was analyzed using ImageJ software (version 1.54 g). Four arbitrarily chosen fields were scored, and the geometric mean fluorescence intensity was calculated. Immunohistochemical (IHC) analysis was performed as described in previous studies [25]. Specimens of tissue underwent overnight incubation at 4 °C utilizing primary antibodies (PRDM16, diluted at 1:100). IHC scores were semi-quantitatively assessed by computing the product of staining strength and the percentage of cells exhibiting positive staining [26].

Preparation of PNPs

Platelet membrane-coated nanoparticles (PNPs) were prepared using emulsified solvent evaporation and ultrasonication techniques, as described in previous studies [27]. Initially, poly(lactic-co-glycolic acid) (PLGA)-encapsulated formononetin was prepared following the methods outlined in our previous research [16]. Platelet membranes were then isolated from mice according to a previously established protocol [28]. In the final step, PLGA-encapsulated formononetin and the pre-prepared platelet membranes were sonicated at 30% amplitude for 10 min to form the platelet membrane-coated nanoparticles (PNPs). The structural features of the microspheres were examined through Transmission Electron Microscopy (TEM, HITACHI HT7800, Japan). The size distribution of the microspheres was evaluated utilizing a Nanoparticle Tracking Analyzer (NTA, Particle Metrix, Germany), with measurements performed three times to verify reproducibility. The electrical surface properties (zeta potential, mV) of the nanoparticles were assessed by employing a Zetasizer Nano ZS particle analyzer (Malvern Instruments).

Statistical analysis

Statistical analysis was executed employing SPSS (version 25.0) and GraphPad Prism (version 9.0) software. Results are denoted as means ± standard deviation (SD). Statistical comparisons between two groups were examined via two-tailed Student's t-tests, whereas multiple group comparisons utilized one-way ANOVA. Statistical significance was set at P-values < 0.05.

Results

Both PRDM16 and pyroptosis were induced by the ferrous myoglobin and glycerol in BUMPT cells and C57BL/6, respectively

The cellular model of RM-induced AKI was established by treating cells with ferrous myoglobin, following previously established protocols [10, 19]. In this study, RT-qPCR and WB analyses suggested that the mRNA and protein levels of PRDM16 were slightly elevated at 6 h, further increased at 12 h, and peaked at 24 h (Fig. 1A–C). These findings were confirmed by immunofluorescence staining, which indicated that PRDM16 was predominantly localized in the nucleus (Fig. 1D and E). Additionally, ROS level and lactate dehydrogenase (LDH) were slightly elevated at 6 h, further elevated at 12 h, and peaked at 24 h, while cell viability decreased at the corresponding time points (Fig. 1F–I). WB also revealed a time-dependent increase in two key pyroptosis proteins, GSDMD and GSDME, following ferrous myoglobin treatment (Fig. 1J–N). To examine the function of pyroptosis in cell viability, BUMPT cells were treated with Disulfiram (DSF), a GSDMD inhibitor. DSF reduced the increase in GSDMD-N and LDH levels induced by ferrous myoglobin and reversed the decrease in cell viability (Supplement Fig. 1A, B, F, and G). Similarly, Z-DEVD-FMK, a Caspase-3-GSDME pathway inhibitor, suppressed the increase in Cleaved Caspase-3, GSDME-N, and LDH levels, while also reversing the loss of cell viability (Supplement Fig. 1C, D, E, H, and I). These findings indicate that pyroptosis serves as a crucial factor in enhancing renal tubular cell damage during ferrous myoglobin treatment.

Glycerol injection is a standard method for establishing an animal model of RM-AKI [20]. In this study, glycerol

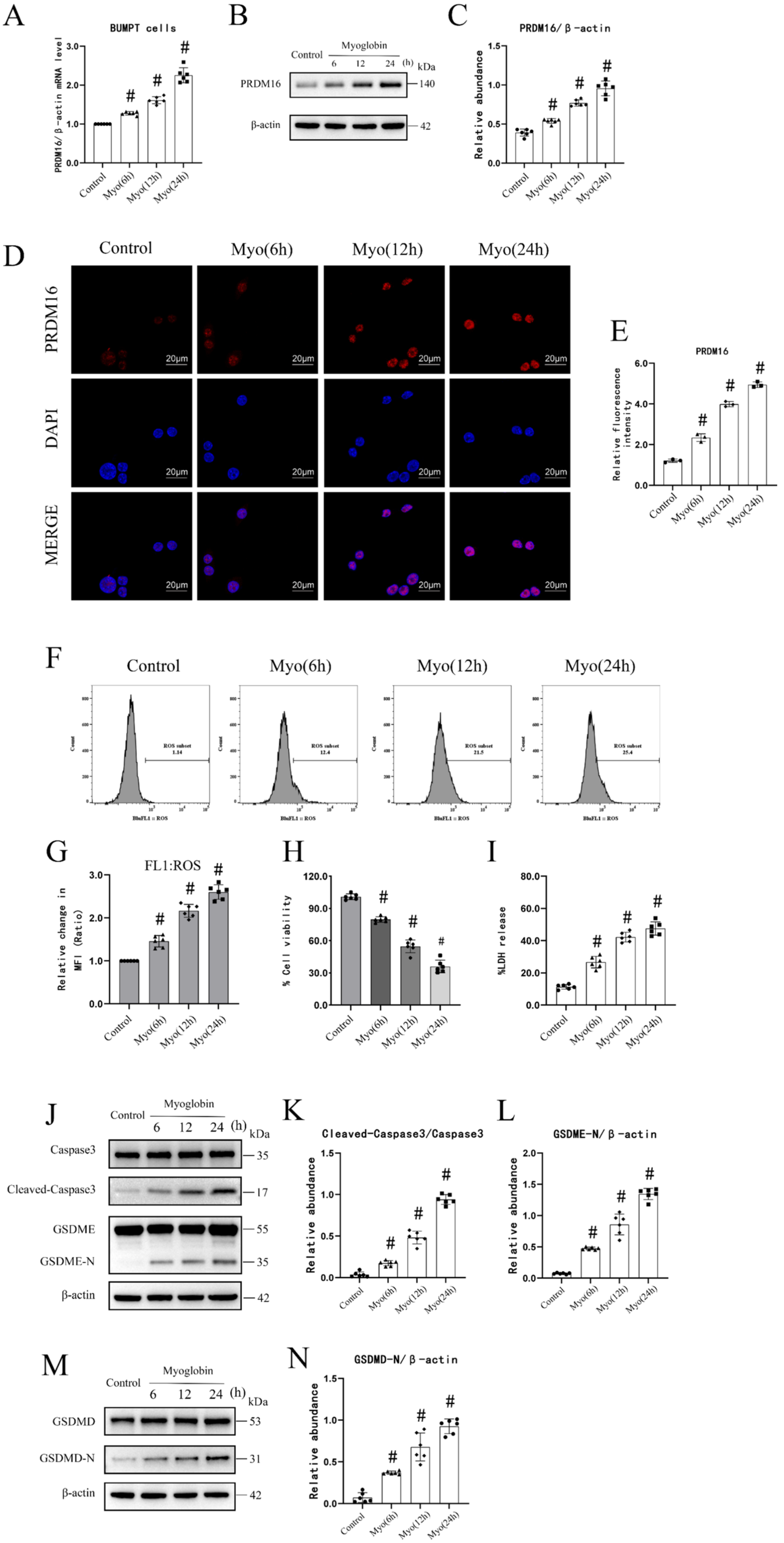

Fig. 1 Ferrous myoglobin induces pyroptosis and upregulates PRDM16 expression in BUMPT cells. BUMPT cells was treated with 200 mM ferrous myoglobin for 6 h, 12 h, 24 h. **A** The RT-qPCR results of PRDM16 in BUMPT cells. **B** The immunoblot analysis of PRDM16 and β-actin in BUMPT cells. **C** Quantification of PRDM16 immunoblot. **D** The expression and localization of PRDM16 in BUMPT cells were analyzed by immunofluorescence, magnification × 600. Scale bar: 20 μm. **E** Relative fluorescence intensity. **F** ROS levels, measured by flow cytometry. **G** Relative change in mean fluorescence intensity (MFI) of ROS levels. **H** Cell viability of BUMPT cells subject to ferrous myoglobin. **I** LDH levels of BUMPT cells subject to ferrous myoglobin. **J** The immunoblot analysis of Cleaved-Caspase3, Caspase3, GSDME and β-actin in BUMPT cells. **K** and **L** Quantification of Cleaved Caspase3. **M** The immunoblot analysis of GSDMD and β-actin in BUMPT cells. **N** Quantification of GSDMD. All data are presented as means ± SD from at least three independent experiments (n = 3 for immunofluorescence experiment; n = 6 for remaining experiments). # indicates significance ($p < 0.05$) versus Control group

treatment led to increased serum blood urea nitrogen (BUN) and creatinine levels at 12 h, with peak values observed at 24 h in C57BL/6 mice (Fig. 2A and B). These findings aligned with the degree of renal tubular damage assessed by HE staining, as well as the increasing trend of mRNA and protein levels of PRDM16 measured by RT-qPCR and WB (Fig. 2C–G). Immunohistochemical staining of PRDM16 further confirmed these findings (Fig. 2H and I). TUNEL and DHE staining demonstrated that glycerol induced renal tubular cell death and the release of ROS at 12 h, peaking at 24 h (Fig. 2J and L). Notably, in line with the results observed in the cellular model, glycerol treatment increased the expression levels of two key pyroptosis proteins, GSDMD and GSDME, as well as Cleaved Caspase-3 (Fig. 2M–Q). These observations collectively indicate that PRDM16 exhibits a connection with pyroptosis in the mouse model of RM-induced AKI.

PRDM16 suppresses the ferrous myoglobin-induced pyroptosis in BUMPT cells

Previous studies have shown that PRDM16 reduces ROS generation and the expression of Cleaved Caspase-3 [29]. ROS production is linked to NLRP3-Caspase-1-GSDMD pathway activation [30–32], while Cleaved Caspase-3 is associated with the activation of GSDME [33–35]. Therefore, it was hypothesized that PRDM16 could regulate both GSDMD and GSDME pyroptosis pathways. To test this hypothesis, BUMPT cells underwent transfection with PRDM16 shRNA and scramble shRNA. RT-qPCR and WB results suggested that PRDM16 shRNA markedly suppressed the mRNA and protein levels of PRDM16 under both saline and ferrous myoglobin treatment conditions (Fig. 3A–C). The data showed that PRDM16 shRNA notably increased ferrous myoglobin-induced ROS generation, LDH release, and IL-1β and IL-18 levels while decreasing cell viability (Fig. 3D–I). Notably, WB analysis revealed that PRDM16 shRNA markedly enhanced the expression of Cleaved Caspase-3, GSDME, NLRP3, Caspase-1-p20, and GSDMD in response to ferrous myoglobin treatment (Fig. 3J–P). Conversely, overexpression of PRDM16 showed an opposite effect, suggesting that PRDM16 has an anti-pyroptosis function through inhibition of both the NLRP3-Caspase1-GSDMD and Caspase3-GSDME axes during ferrous myoglobin treatment (Fig. 4).

PRDM16 binds to the promoter region of USP10 and promotes transcription

Since PRDM16 is a transcription factor that regulates gene transcription, its anti-pyroptosis mechanism was explored. Our recent ChIP-seq study of a DOX-induced HA-PRDM16 stable cell line was examined [18]. Among the sequencing results, USP10 stood out, one recent study found that USP10 regulates PANoptosis by suppressing GSDMD and GSDME in tumor cell lines [36]. By visualizing the ChIP-seq data using IGV, a significantly higher enrichment of PRDM16 was observed at the USP10 promoter (Fig. 5A). Additionally, data from publicly available databases of intestinal tissue further confirmed that PRDM16 is enriched at the USP10 promoter region [21] (Fig. 5B). Using the online tool MoloTool (Motif Location Toolbox, http://molotool.autosome.ru), identified two potential binding sites of PRDM16 on the USP10 promoter region, designated as P1 and P2 (Fig. 5C and D). Subsequently, ChIP-PCR and ChIP-qPCR results confirmed that PRDM16 binds to both sites of the USP10 promoter (Fig. 5E and F). A time-dependent rise in USP10 level was noted following treatment with ferrous myoglobin (Fig. 5G–I). Furthermore, WB analysis suggested that USP10 level was reduced upon PRDM16 knockdown (Fig. 5J–L), while overexpression of PRDM16 enhanced USP10 expression (Fig. 5M–O). These results suggest that PRDM16 directly binds to and positively regulates USP10 expression.

USP10 inhibits the ferrous myoglobin-induced pyroptosis in BUMPT cells

Although the above findings established USP10 as a downstream target of PRDM16, the function and precise mechanism by which PRDM16 modulates pyroptosis remain largely unclear. Earlier research has demonstrated that USP10 diminishes ROS production and decreases Cleaved Caspase-3 levels [37–42]. One study also found that USP10 regulates PANoptosis by suppressing GSDMD and GSDME in tumor cell lines [36]. These studies suggest that USP10 may be associated with pyroptosis. In the current study, USP10 expression in BUMPT cells was knocked down using USP10 shRNA under both saline and ferrous myoglobin treatment conditions (Fig. 6A–C). The data showed that USP10 shRNA induced cellular ROS generation, LDH release, elevated levels of IL-1β and IL-18, and diminished cell viability during ferrous myoglobin treatment (Fig. 6D–I). Notably, WB analysis revealed that USP10 shRNA significantly enhanced the level of Cleaved Caspase-3, GSDME, NLRP3, Caspase-1-p20, and GSDMD in response to ferrous myoglobin treatment (Fig. 6J–P). In contrast, overexpression of USP10 exhibited an opposite effect, suggesting that USP10 has an anti-pyroptosis function by inhibiting both the NLRP3-Caspase-1-GSDMD and Caspase-3-GSDME axes during ferrous myoglobin treatment (Fig. 7).

Fig. 2 PRDM16 is upregulated and pyroptosis is triggered in RM-AKI mice. Wild-type mice were injected with 50% glycerol to establish a rhabdomyolysis-associated acute kidney injury (RM-AKI) model, mice were sacrificed at 12 h and 24 h. **A** Serum Creatinine of mice. **B** Serum Blood Urea Nitrogen of mice. **C** Hematoxylin–eosin staining of mouse kidney. **D** Tubular damage score of mouse kidney. **E** RT-qPCR quantification of PRDM16 in mouse kidney. **F** The immunoblot analysis of PRDM16 and β-actin in mouse kidney. G Quantitative analysis of immunoblot band density. **H** Immunohistochemical staining of PRDM16. **I** Quantification analysis of PRDM16 staining. **J** Representative regions of TUNEL-positive staining and DHE staining. **K** and **L** Quantification of TUNEL-positive staining and DHE staining. **M** The immunoblot analysis of Cleaved-Caspase3, Caspase3, GSDME and β-actin in mouse kidney. **N** and **O** Quantification of Cleaved-Caspase3 and GSDME. (P) The immunoblot analysis of GSDMD in mouse kidney. **Q** The quantification of GSDMD. Data are presented as means ± SD from six independent experiments (n = 6). # indicates significance ($p < 0.05$) versus Control group (glycerol 0 h group)

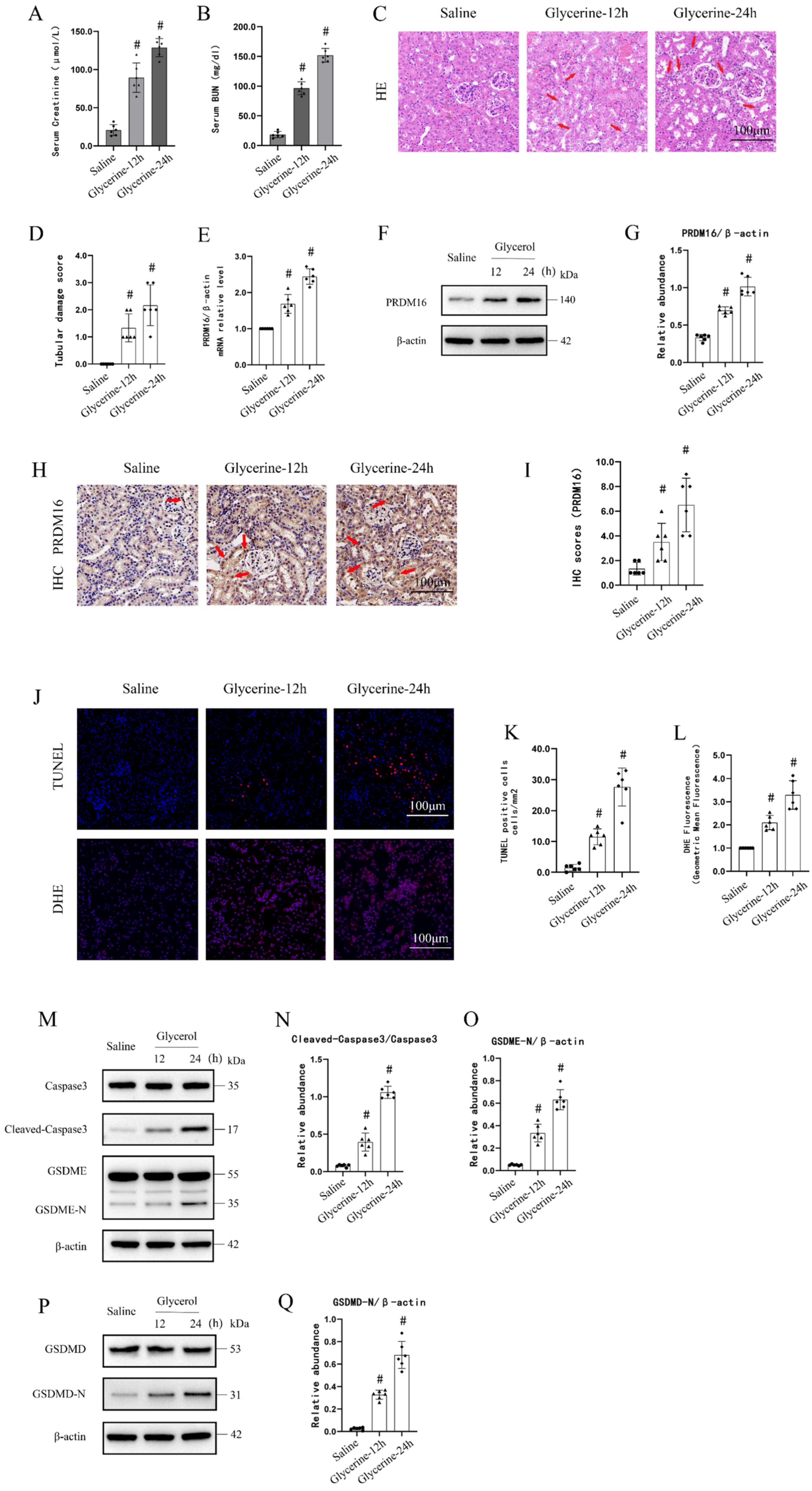

Fig. 3 Downregulation of PRDM16 exacerbates pyroptosis in BUMPT cells. BUMPT cells were transfected with PRDM16 shRNA or scramble shRNA, followed by treatment with saline or ferrous myoglobin for 24 h. **A** Relative quantitative of RT-qPCR of PRDM16 in BUMPT cells. **B** Immunoblot analysis for PRDM16 and β-actin. **C** Quantitative analysis of PRDM16 immunoblot bands. **D** Levels of ROS as measured by flow cytometry. **E** Relative change in mean fluorescence intensity (MFI) of ROS levels. **F** Cell viability of BUMPT cells. **G** LDH level. **H** and **I** IL-1b and IL-18 levels measured by ELISA assay. **J** The immunoblot of Cleaved-Caspase3, Caspase3, GSDME and β-actin. **K** and **L** The quantification of Cleaved-Caspase3 and GSDME immunoblot results. **M** The immunoblot of NLRP3, Caspase1-p20, GSDMD and β-actin. **N**–**P** The quantification of NLRP3, Caspase1-p20, GSDMD immunoblot results. Data are presented as means ± SD (n = 4 for IL-1b and IL-18 levels; n = 6 for remaining experiments). # indicates significance ($p < 0.05$) versus scramble/Saline group. * indicates significance ($p < 0.05$) versus scramble/myoglobin group

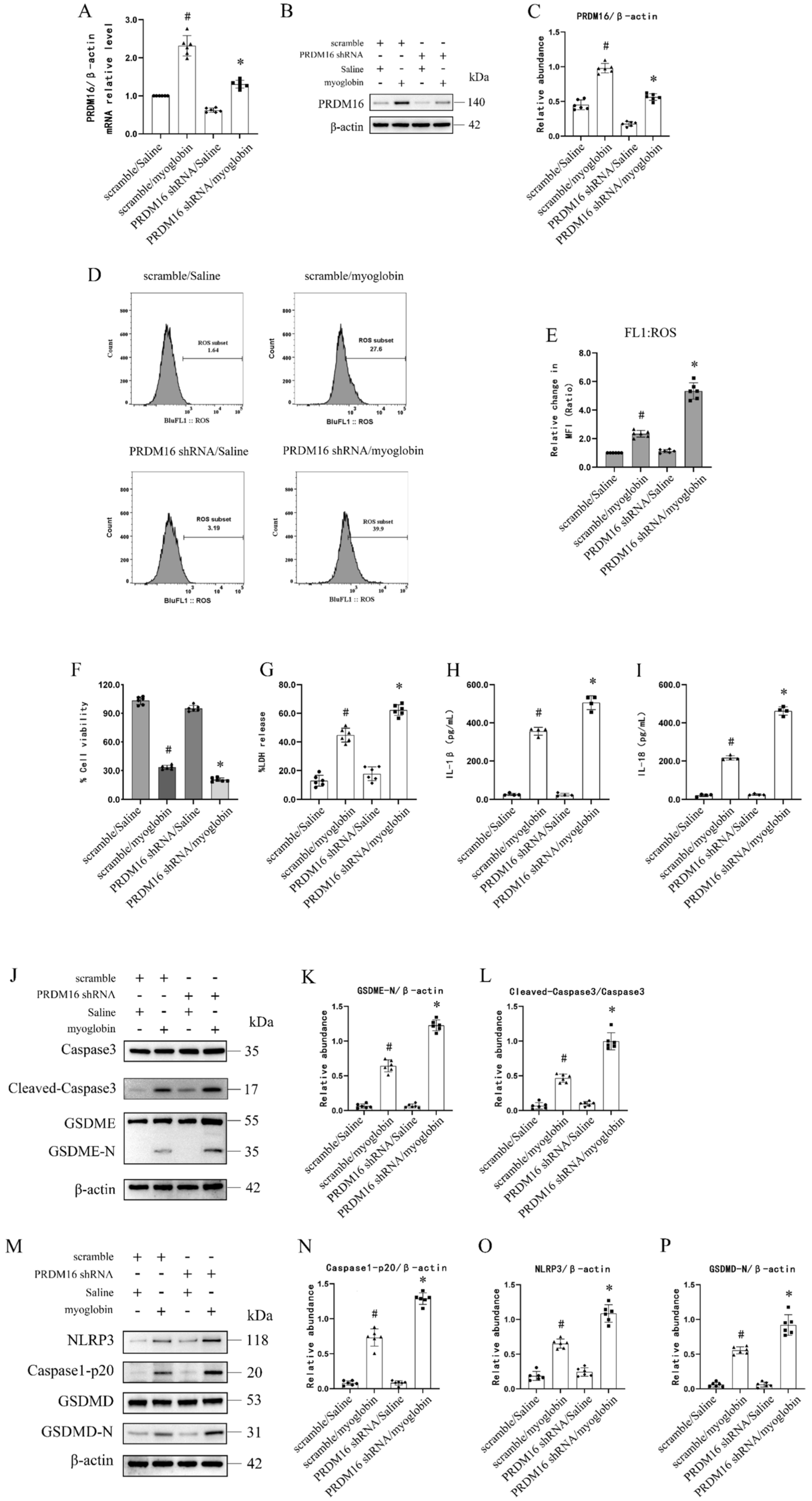

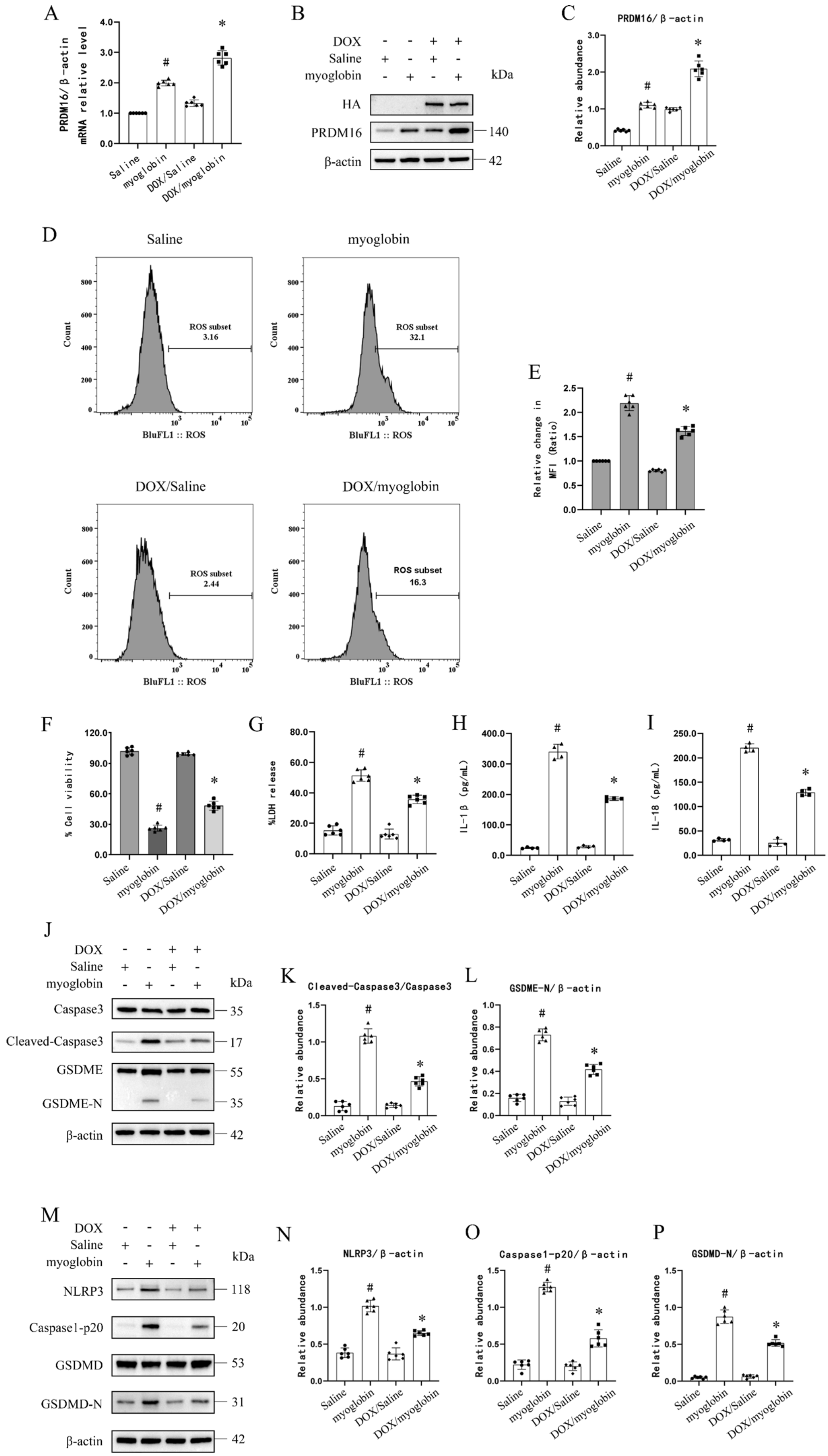

Fig. 4 Upregulation of PRDM16 protects BUMPT cells against pyroptosis. Doxycycline (DOX)-induced HA-PRDM16 stable cell line treated with saline or ferrous myoglobin. **A** Relative quantitative of RT-qPCR of PRDM16 in BUMPT cells. **B** Immunoblot analysis for PRDM16 and β-actin. **C** Quantitative analysis of PRDM16 immunoblot bands. **D** Levels of ROS as measured by flow cytometry. **E** Relative change in mean fluorescence intensity (MFI) of ROS levels. **F** Cell viability of BUMPT cells. **G** LDH level. **H** and **I** IL-1b and IL-18 levels measured by ELISA assay. **J** The immunoblot of Cleaved-Caspase3, Caspase3, GSDME and β-actin. **K** and **L** The quantification of Cleaved-Caspase3 and GSDME immunoblot results. **M** The immunoblot of NLRP3, Caspase1-p20, GSDMD and β-actin. **N**–**P** The quantification of NLRP3, Caspase1-p20, GSDMD immunoblot results. Data are presented as means ± SD (n = 4 for IL-1b and IL-18 levels; n = 6 for remaining experiments). # indicates significance ($p < 0.05$) versus Saline group. * indicates significance ($p < 0.05$) versus myoglobin group

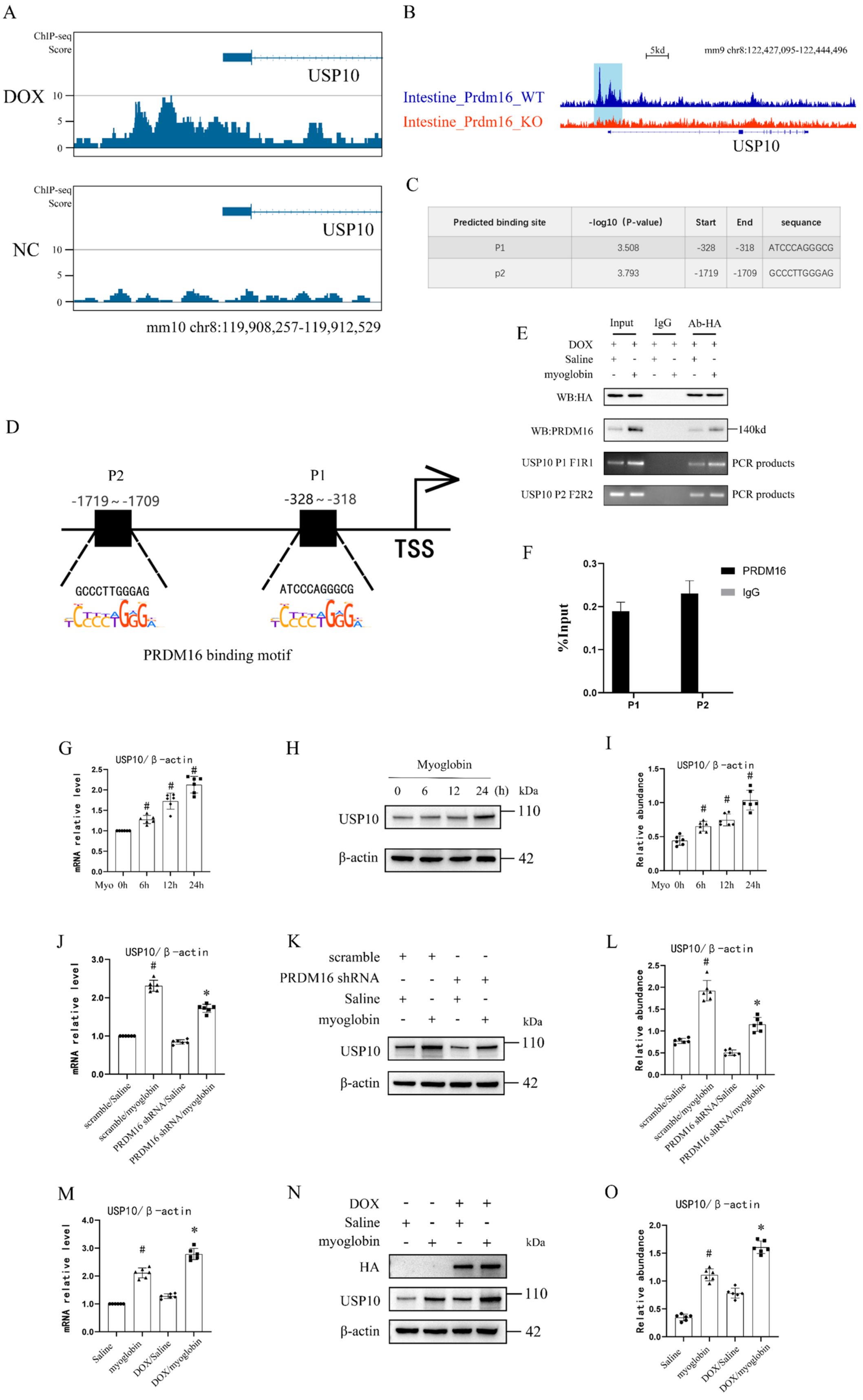
A
ChIP-seq Score
DOX
USP10
10
5
0
NC
mm10 chr8:119,908,257-119,912,529
B
5kd
mm9 chr8:122,427,095-122,444,496
Intestine_Prdm16_WT
Intestine_Prdm16_KO
USP10
C
Predicted binding site | -log10 (P-value) | Start | End | sequance
P1 | 3.508 | -328 | -318 | ATCCCAGGGCG
p2 | 3.793 | -1719 | -1709 | GCCCTTGGGAG
D
P2
-1719 ~ -1709
P1
-328 ~ -318
TSS
GCCCTTGGGAG
ATCCCAGGGCG
PRDM16 binding motif
E
Input
IgG
Ab-HA
DOX
Saline
myoglobin
WB:HA
WB:PRDM16
140kd
USP10 P1 F1R1
USP10 P2 F2R2
PCR products
F
%Input
0.3
0.2
0.1
0.0
P1
P2
PRDM16
IgG
G
USP10/ β-actin
mRNA relative level
Myo 0h 6h 12h 24h
H
Myoglobin
0 6 12 24 (h)
kDa
USP10
β-actin
110
42
I
USP10/ β-actin
Relative abundance
Myo 0h 6h 12h 24h
J
USP10/ β-actin
mRNA relative level
scramble/Saline
scramble/myoglobin
PRDM16 shRNA/Saline
PRDM16 shRNA/myoglobin
K
scramble
PRDM16 shRNA
Saline
myoglobin
kDa
USP10
β-actin
110
42
L
USP10/ β-actin
Relative abundance
scramble/Saline
scramble/myoglobin
PRDM16 shRNA/Saline
PRDM16 shRNA/myoglobin
M
USP10/ β-actin
mRNA relative level
Saline
myoglobin
DOX/Saline
DOX/myoglobin
N
DOX
Saline
myoglobin
kDa
HA
USP10
β-actin
110
42
O
USP10/ β-actin
Relative abundance
Saline
myoglobin
DOX/Saline
DOX/myoglobin

◂**Fig. 5** PRDM16 binds to the promoter region of USP10 and promotes transcription. **A** ChIP-seq image of doxycycline (DOX)-induced HA- PRDM16 stable cell visualized in IGV. **B** ChIP-seq image of PRDM16-knock out mice and wild type mice, data from publicly available datasets (GSE131487). **C** and **D** Visualization of PRDM16 binding site on USP10 gene promoter predicted by Molo-Tool database. **E** ChIP-PCR assays showing the binding of PRDM16 to the P1 and P2 region of USP10 gene promoter. **F** ChIP-qPCR assays. **G** The RT-qPCR results of USP10 in BUMPT cells with ferrous myoglobin treatment duration. **H** and **I** The immunoblot analysis and quantification of USP10 in BUMPT cells with ferrous myoglobin treatment duration. BUMPT cells were transfected with PRDM16 shRNA and treated with ferrous myoglobin. **J** RT-qPCR results of USP10 mRNA. **K** and **L** The immunoblot analysis and quantification of USP10. Doxycycline (DOX)-induced HA-PRDM16 stable cell overexpressing PRDM16 and treated with ferrous myoglobin. **M** RT-qPCR results of USP10 mRNA. **N** and **O** The immunoblot analysis and quantification of USP10. Data are presented as means ± SD (n = 6). # indicates significance ($p < 0.05$) versus Myoglobin 0 h group, scramble/Saline group or Saline group. * indicates significance ($p < 0.05$) versus scramble/myoglobin group or myoglobin group

PRDM16-mediated pyroptosis resistance in BUMPT cells is dependent on USP10

To further confirm whether the anti-pyroptosis function of PRDM16 depends on USP10, USP10 shRNA was transfected into a DOX-induced HA-PRDM16 stable cell line. The experimental groups were divided into five conditions: control, myoglobin, DOX/myoglobin, USP10 shRNA/myoglobin, and DOX + USP10 shRNA/myoglobin. RT-qPCR and WB confirmed that USP10 shRNA effectively suppressed the mRNA and protein expression of USP10, while DOX successfully induced PRDM16 expression (Fig. 8A–E). The outcomes showed that DOX/myoglobin treatment markedly suppressed the ferrous myoglobin-induced increase of ROS, Cleaved Caspase-3, GSDME, NLRP3, Caspase-1-p20, and GSDMD, but these changes were reversed by transfection with USP10 shRNA (Fig. 8F–N). As a reverse validation, PRDM16 shRNA and USP10 plasmid were simultaneously transfected into BUMPT cells. Five experimental groups were classified according to treatment conditions: control, myoglobin, PRDM16 shRNA/myoglobin, USP10 plasmid/myoglobin, and PRDM16 shRNA + USP10 plasmid/myoglobin. Transfection with the USP10 plasmid resulted in elevated mRNA and protein expression of USP10, while PRDM16 shRNA effectively suppressed USP10 expression (Supplement Fig. 2A–E). The data showed that PRDM16 shRNA markedly enhanced the ferrous myoglobin-induced increase of ROS, Cleaved Caspase-3, GSDME, NLRP3, Caspase-1-p20, and GSDMD, which was reversed by overexpression of USP10 (Supplement Fig. 2F–N). Collectively, these results suggest that USP10 mediates the anti-pyroptosis role of PRDM16 during ferrous myoglobin treatment in BUMPT cells.

PRDM16 protested the progression of rhabdomyolysis-induced AKI via suppression of USP10/NLRP3-Caspase1-GSDMD as well as the Caspase3-GSDME axes

To verify the in vitro findings, proximal tubule-PRDM16-knockout (PT-PRDM16-KO) and knock-in (PT-PRDM16-KI) mice were employed as described in previous studies [15, 16, 18]. These mice were subjected to glycerol or saline treatment for 24 h. The glycerol treatment induced an elevation of BUN and creatinine (Fig. 9D and E), as well as increased ROS generation (Fig. 9F and H), renal tubular damage (Fig. 9F and G), enhanced apoptosis (Fig. 9F and I), and upregulation of Cleaved Caspase-3, GSDME, NLRP3, Caspase-1-p20, and GSDMD (Fig. 9J–P). These effects were further exacerbated in PT-PRDM16-KO mice. Conversely, PT-PRDM16-KI mice exhibited the opposite results to PT-PRDM16-KO (Fig. 10). These results suggest that PRDM16 suppresses pyroptosis and ameliorates the development of RM-AKI through inhibition of the USP10/NLRP3-Caspase-1-GSDMD and Caspase-3-GSDME axes.

PNPs-encapsulated formononetin attenuates pyroptosis and renal injury in RM-AKI

Our recent exploration identified that formononetin, a phytoestrogen derived from the leaves of red clover, binds to and induces PRDM16 levels in diabetic kidney disease (DKD). Nevertheless, formononetin exhibits restricted bioavailability, and its application has primarily focused on preventive measures instead of therapeutic interventions. To overcome this limitation, PNPs were utilized, as they exhibit superior biocompatibility and controlled drug release properties, facilitating the rapid release of formononetin. Platelet membranes and PLGA (poly(lactic-co-glycolic acid)) were used to form PNPs, which encapsulated formononetin and were administered via tail vein injection 30 min after glycerol treatment (Fig. 11A). TEM revealed that the PNPs had a well-dispersed spherical morphology with a distinct outer envelope (Fig. 11B). NTA showed that the average particle size of PNPs was larger than that of PLGA alone (Fig. 11C and D). Furthermore, the zeta potential of PNPs was altered after modification with platelet membranes (Fig. 11E). WB analysis confirmed the presence of platelet membrane protein CD62p in both the platelet membrane (PM) and PNPs (Fig. 11F). After administration of various doses of PNPs-encapsulated formononetin via tail vein for 24 h, the expression of PRDM16 was slightly increased at a concentration of 10 mg/kg of PNPs, peaked at 20 mg/kg and declined at 30 and 40 mg/kg (Fig. 11G and H). Following administration of a 20 mg/kg injection in mice, PRDM16 levels exhibited a progressive elevation, stabilizing after four hours (Fig. 11I and J). Glycerol treatment induced the elevation of BUN and

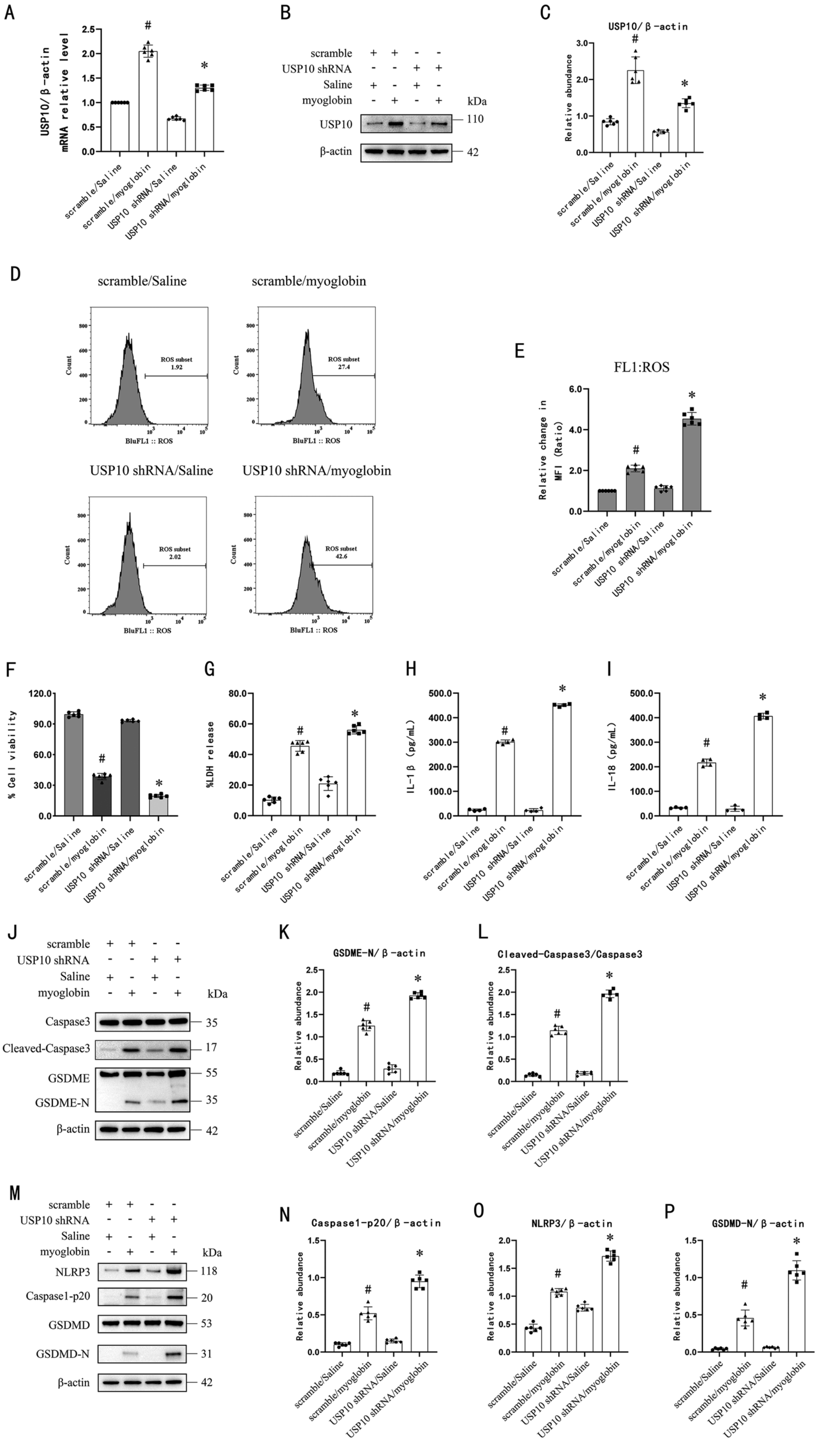

Fig. 6 Downregulation of USP10 exacerbates pyroptosis in BUMPT cells. BUMPT cells were transfected with USP10 shRNA or scramble shRNA, followed by treatment with saline or ferrous myoglobin for 24 h. **A** Relative quantitative of RT-qPCR of USP10 in BUMPT cells. **B** Immunoblot analysis for USP10 and β-actin. **C** Quantitative analysis of USP10 immunoblot bands. **D** Levels of ROS as measured by flow cytometry. **E** Relative change in mean fluorescence intensity (MFI) of ROS levels. **F** Cell viability of BUMPT cells. **G** LDH level. **H** and **I** IL-1b and IL-18 levels measured by ELISA assay. **J** The immunoblot of Cleaved-Caspase3, Caspase3, GSDME and β-actin. **K** and **L** The quantification of Cleaved-Caspase3 and GSDME immunoblot results. **M** The immunoblot of NLRP3, Caspase1-p20, GSDMD and β-actin. **N**–**P** The quantification of NLRP3, Caspase1-p20, GSDMD immunoblot results. Data are presented as means ± SD (n = 4 for IL-1b and IL-18 levels; n = 6 for remaining experiments). # indicates significance ($p < 0.05$) versus scramble/Saline group. * indicates significance ($p < 0.05$) versus scramble/myoglobin group

Fig. 7 Upregulation of USP10 protects BUMPT cells against pyroptosis. BUMPT cells were transfected with USP10 Plasmid or empty Plasmid, followed by treatment with saline or ferrous myoglobin for 24 h. **A** Relative quantitative of RT-qPCR of USP10 in BUMPT cells. **B** Immunoblot analysis for USP10 and β-actin. **C** Quantitative analysis of USP10 immunoblot bands. **D** Levels of ROS as measured by flow cytometry. **E** Relative change in mean fluorescence intensity (MFI) of ROS levels. **F** Cell viability of BUMPT cells. **G** LDH level. **H** and **I** IL-1b and IL-18 levels measured by ELISA assay. **J** The immunoblot of Cleaved-Caspase3, Caspase3, GSDME and β-actin. **K** and **L** The quantification of Cleaved-Caspase3 and GSDME immunoblot results. **M** The immunoblot of NLRP3, Caspase1-p20, GSDMD and β-actin. **N**–**P** The quantification of NLRP3, Caspase1-p20, GSDMD immunoblot results. Data are presented as means ± SD (n = 4 for IL-1b and IL-18 levels; n = 6 for remaining experiments). # indicates significance (p < 0.05) versus Empty Plasmid/Saline group. * indicates significance (p < 0.05) versus Empty Plasmid/myoglobin group

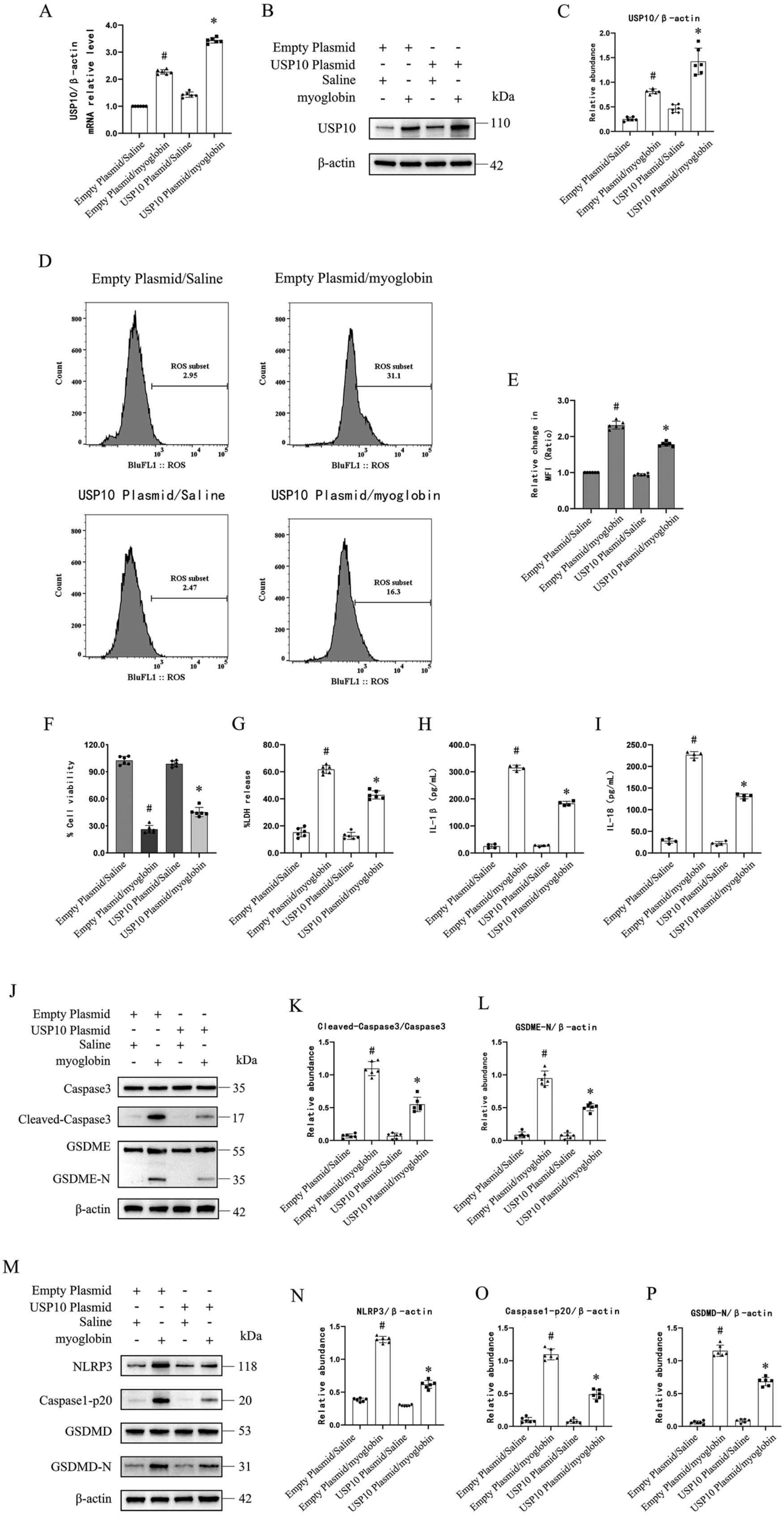

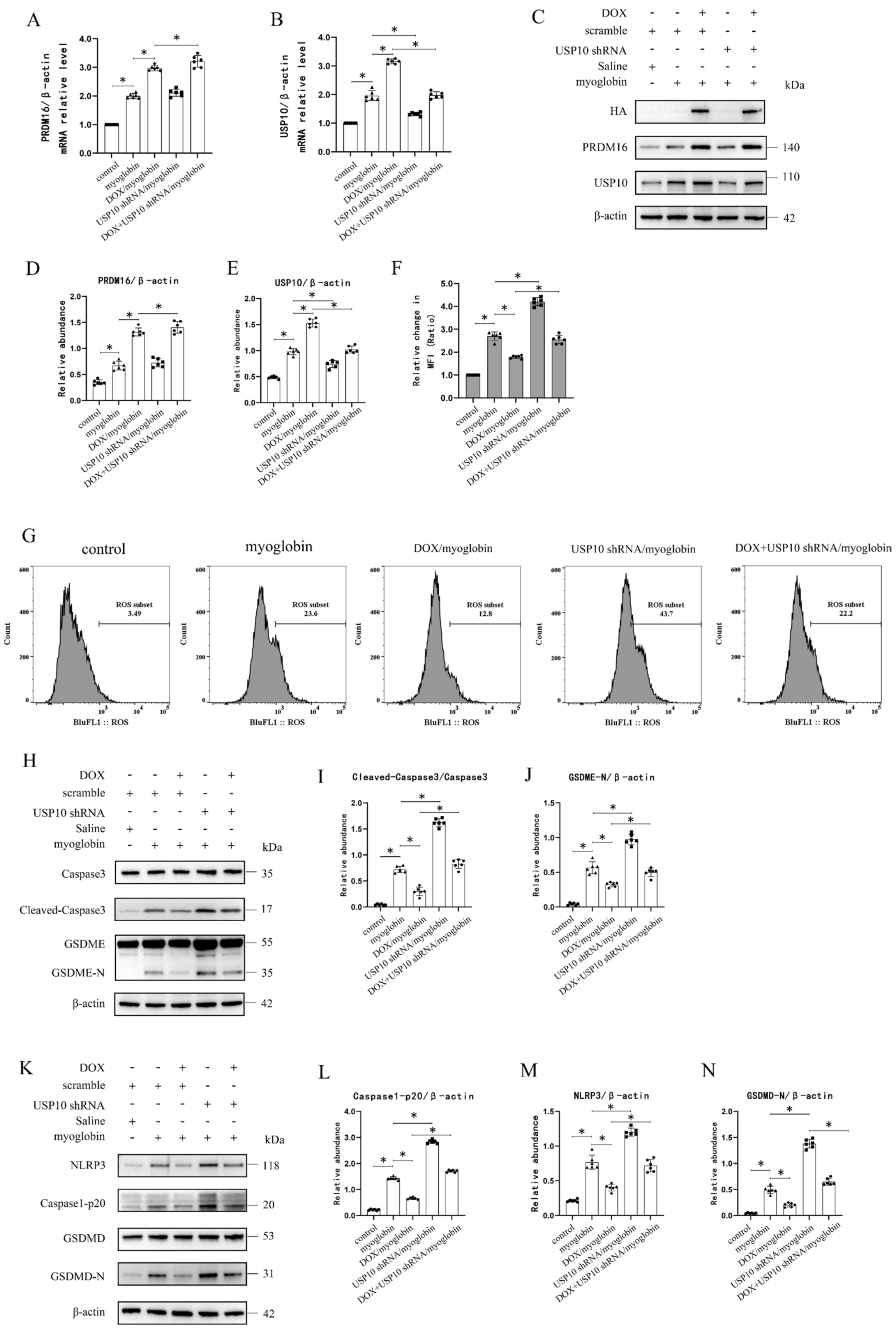
A
PRDM16/β-actin mRNA relative level
B
USP10/β-actin mRNA relative level
C
DOX - - + - +
scramble + + + - -
USP10 shRNA - - - + +
Saline + - - - -
myoglobin - + + + +
kDa
HA
PRDM16 140
USP10 110
β-actin 42
D
PRDM16/β-actin
Relative abundance
E
USP10/β-actin
Relative abundance
F
Relative change in MFI (Ratio)
G
control
myoglobin
DOX/myoglobin
USP10 shRNA/myoglobin
DOX+USP10 shRNA/myoglobin
ROS subset 3.49
ROS subset 23.6
ROS subset 12.8
ROS subset 43.7
ROS subset 22.2
Count
BluFL1 :: ROS
H
DOX - - + - +
scramble + + + - -
USP10 shRNA - - - + +
Saline + - - - -
myoglobin - + + + +
kDa
Caspase3 35
Cleaved-Caspase3 17
GSDME 55
GSDME-N 35
β-actin 42
I
Cleaved-Caspase3/Caspase3
Relative abundance
J
GSDME-N/β-actin
Relative abundance
K
DOX - - + - +
scramble + + + - -
USP10 shRNA - - - + +
Saline + - - - -
myoglobin - + + + +
kDa
NLRP3 118
Caspase1-p20 20
GSDMD 53
GSDMD-N 31
β-actin 42
L
Caspase1-p20/β-actin
Relative abundance
M
NLRP3/β-actin
Relative abundance
N
GSDMD-N/β-actin
Relative abundance
control
myoglobin
DOX/myoglobin
USP10 shRNA/myoglobin
DOX+USP10 shRNA/myoglobin
*

◂**Fig. 8** Overexpression of PRDM16 attenuated cellular pyroptosis, which was antagonized by suppression of USP10. Doxycycline (DOX)-induced HA-PRDM16 stable BUMPT cell line was transfected with USP10 shRNA, followed by treatment with ferrous myoglobin for 24 h. **A** and **B** Relative quantitative of RT-qPCR of PRDM16 and USP10 in BUMPT cells. **C** Immunoblot analysis for USP10, PRDM16 and β-actin. **D** and **E** Quantitative analysis of PRDM16 and USP10 immunoblot bands. **F** Relative change in mean fluorescence intensity (MFI) of ROS levels. **G** ROS Levels measured by flow cytometry. **H** The immunoblot of Cleaved-Caspase3, Caspase3, GSDME and β-actin. **I** and The quantification of Cleaved-Caspase3 and GSDME immunoblot results. **K** The immunoblot of NLRP3, Caspase1-p20, GSDMD and β-actin. **L–N** The quantification of NLRP3, Caspase1-p20, GSDMD immunoblot results. Data are presented as means ± SD (n = 6). * Indicates significance of comparison between two groups ($p < 0.05$)

creatinine (Fig. 11K and L), as well as increased ROS generation (Fig. 11M and O), renal tubular damage (Fig. 11M and N), apoptosis (Fig. 11M and P), and upregulation of Cleaved Caspase-3, GSDME, NLRP3, Caspase-1-p20, and GSDMD (Supplement Fig. 3M). However, these changes were attenuated by PNPs-coated formononetin at the 20 mg/kg dose. The findings indicate that PNPs-coated formononetin demonstrates therapeutic potential in alleviating renal injury and attenuating pyroptosis in RM-AKI mice by targeting PRDM16 to suppress the USP10/NLRP3-Caspase-1-GSDMD and Caspase-3-GSDME axes.

Discussion

Previous studies have demonstrated that PRDM16 protects against the development of AKI induced by cisplatin, ischemia, and sepsis [15, 16]. In line with these findings, the present study reveals, for the first time, that PRDM16 inhibits pyroptosis to alleviate renal tubular injury in vitro. Mechanistically, PRDM16 binds to the USP10 promoter, promoting its transcription, which in turn suppresses the USP10/NLRP3-Caspase1-GSDMD and Caspase3-GSDME signaling pathways. Moreover, PT-PRDM16-KI mice and PNPs-coated formononetin significantly attenuated the progression of RM-induced AKI, offering a potential therapeutic approach for this condition.

PRDM16, a zinc finger transcription factor, is widely known for its role in the biogenesis of brown and beige adipocytes [43–45]. However, its function in regulating cell death has received limited attention. Recent studies have shown that PRDM16 mitigates renal tubular apoptosis and ferroptosis induced by cisplatin, ischemia, and sepsis [15, 16], suggesting its protective role against renal tubular cell death. Pyroptosis, a pro-inflammatory form of programmed cell death, plays a critical role in the progression of AKI, often driven by NF-κB activation, mitochondrial dysfunction, and excessive endoplasmic reticulum (ER) stress [12, 46]. Notably, the current study demonstrates that PRDM16 suppresses pyroptosis induced by ferrous myoglobin and glycerol in vitro and in vivo (Figs. 3, 4, 9, and 10), further reinforcing the previous evidence that PRDM16 functions as a suppressor of cell death.

Ubiquitin-specific peptidase 10 (USP10), a member of the deubiquitinase family, removes ubiquitin from proteins. The role of USP10 in kidney diseases remains underexplored. Two studies have shown that USP10 suppresses ROS generation and renal cell apoptosis in sepsis-induced AKI [42, 47]. Furthermore, one study reported that USP10 regulates PANoptosis by inhibiting GSDMD and GSDME in tumor cell lines [36], suggesting its potential involvement in pyroptosis. Notably, our data provide the first evidence that USP10 inhibits pyroptosis induced by ferrous myoglobin by suppressing the NLRP3-Caspase1-GSDMD and Caspase3-GSDME axes (Figs. 6 and 7). Additionally, USP10 was regulated by PRDM16, and its function aligned with that of PRDM16. Collectively, the findings show that PRDM16 upregulates USP10 expression, thereby suppressing pyroptosis through inhibition of the NLRP3-Caspase1-GSDMD and Caspase3-GSDME axes.

Previous studies suggested that ferromentin pretreatment could protect against the progression of DKD and AKI induced by ischemia and cisplatin by upregulating PRDM16 [15, 18]. Further investigations using PLGA-coated ferromentin demonstrated its efficacy in sepsis-induced AKI treatment [16]. However, some studies have reported that nanoparticles lacking a cell membrane layer are prone to rapid clearance from the body [48]. Interestingly, PNPs can overcome this limitation, exhibiting platelet-like binding properties for collagen and damaged vascular areas [49–54]. Two studies found that PNPs targeted AKI injury sites and were retained in the body for extended periods [28, 55]. The current study demonstrated that PNPs-coated ferromentin significantly alleviated RM-induced pyroptosis and AKI progression by targeting PRDM16 to suppress the NLRP3-Caspase1-GSDMD and Caspase3-GSDME axes (Fig. 11).

Despite the encouraging findings of our study, some limitations remain. First, although we identified a regulatory role for USP10 in pyroptosis, the exact molecular mechanisms of this process remain to be elucidated and require further comprehensive studies. Second, the lack of validation of clinical samples is a limitation, as it limits the translational relevance and applicability of our findings in clinic. Third, a systematic investigation of the stability characteristics of platelet membrane-encapsulated nanoparticles in vitro is needed, especially their optimal storage time and conditions, which are crucial factors for their potential therapeutic applications.

The establishment of animal model for Rhabdomyolysis-associated Acute Kidney Injury (AKI) can be achieved through two primary methodologies: glycerol muscle injection and non-invasive physical crush injury (e.g.,

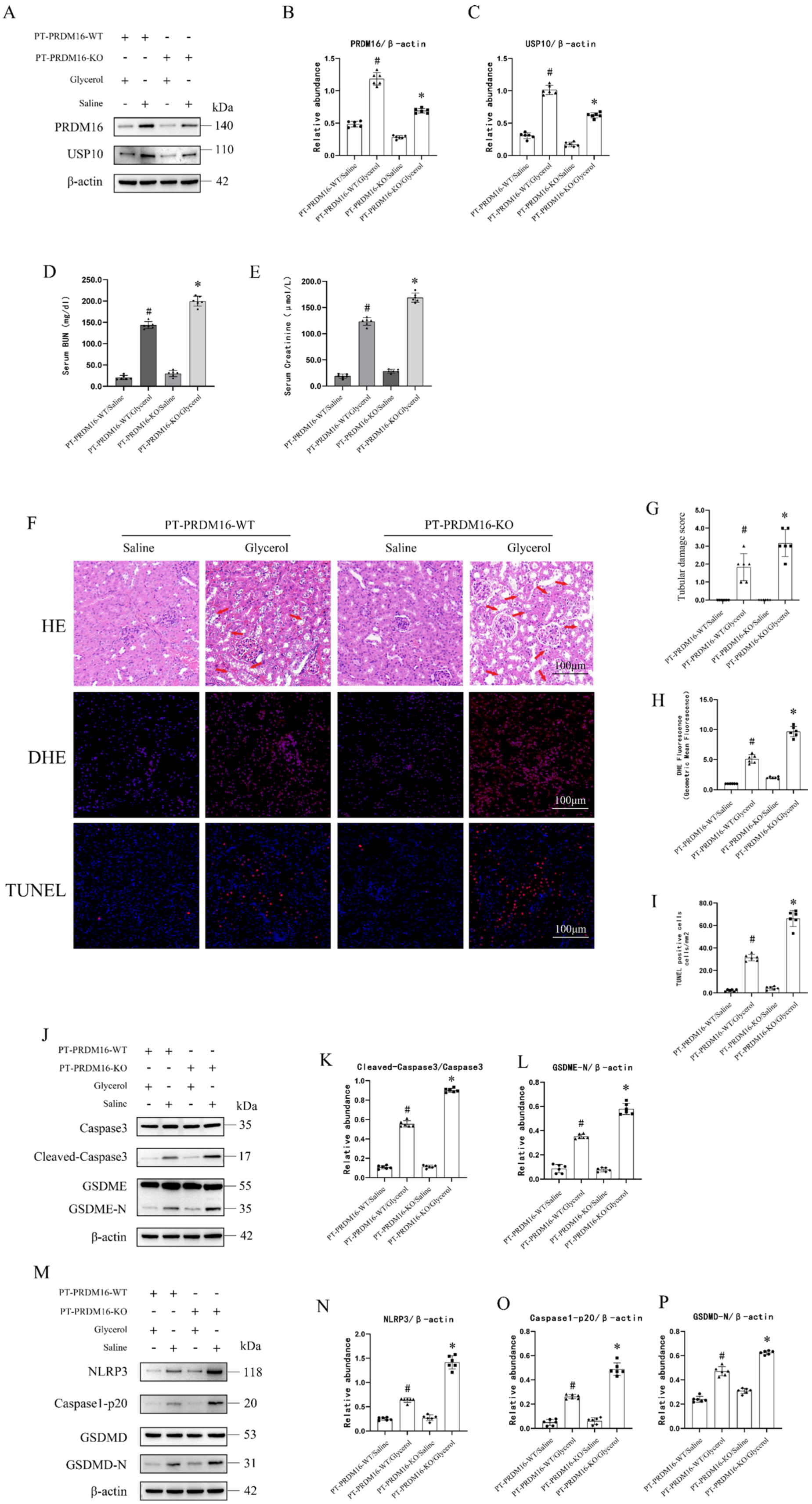

Fig. 9 Renal injury and pyroptosis exacerbated in PT-PRDM16-KO RM-AKI mice. Wild-type mice and PT-PRDM16-KO mice were injected with 50% glycerol to establish rhabdomyolysis-associated acute kidney injury (RM-AKI) model, mice were sacrificed at 24 h. **A** The immunoblot analysis of PRDM16, USP10 and β-actin in mouse kidney. **B** and **C** Quantitative analysis of PRDM16 and USP10 immunoblot band density. **D** The levels of serum BUN in mice. **E** The levels of serum Creatinine in mice. **F** Representative regions of Hematoxylin–eosin staining, Dihydroethidium staining and TUNEL staining of mouse kidney. **G** Tubular damage score of mouse kidney. **H** Quantification of DHE staining. **I** Quantification of TUNEL-positive staining. **J** The immunoblot analysis of Cleaved-Caspase3, Caspase3, GSDME and β-actin in mouse kidney. **K** and **L** Quantification of Cleaved-Caspase3 and GSDME. **M** The immunoblot analysis of NLRP3, Caspase1-p20 and GSDMD in mouse kidney. **N**–**P** The quantification of NLRP3, Caspase1-p20 and GSDMD. Data are presented as means ± SD (n = 6). # indicates significance ($p < 0.05$) versus PT-PRDM16-WT/Saline group. * indicates significance ($p < 0.05$) versus PT-PRDM16-WT/ Glycerol group

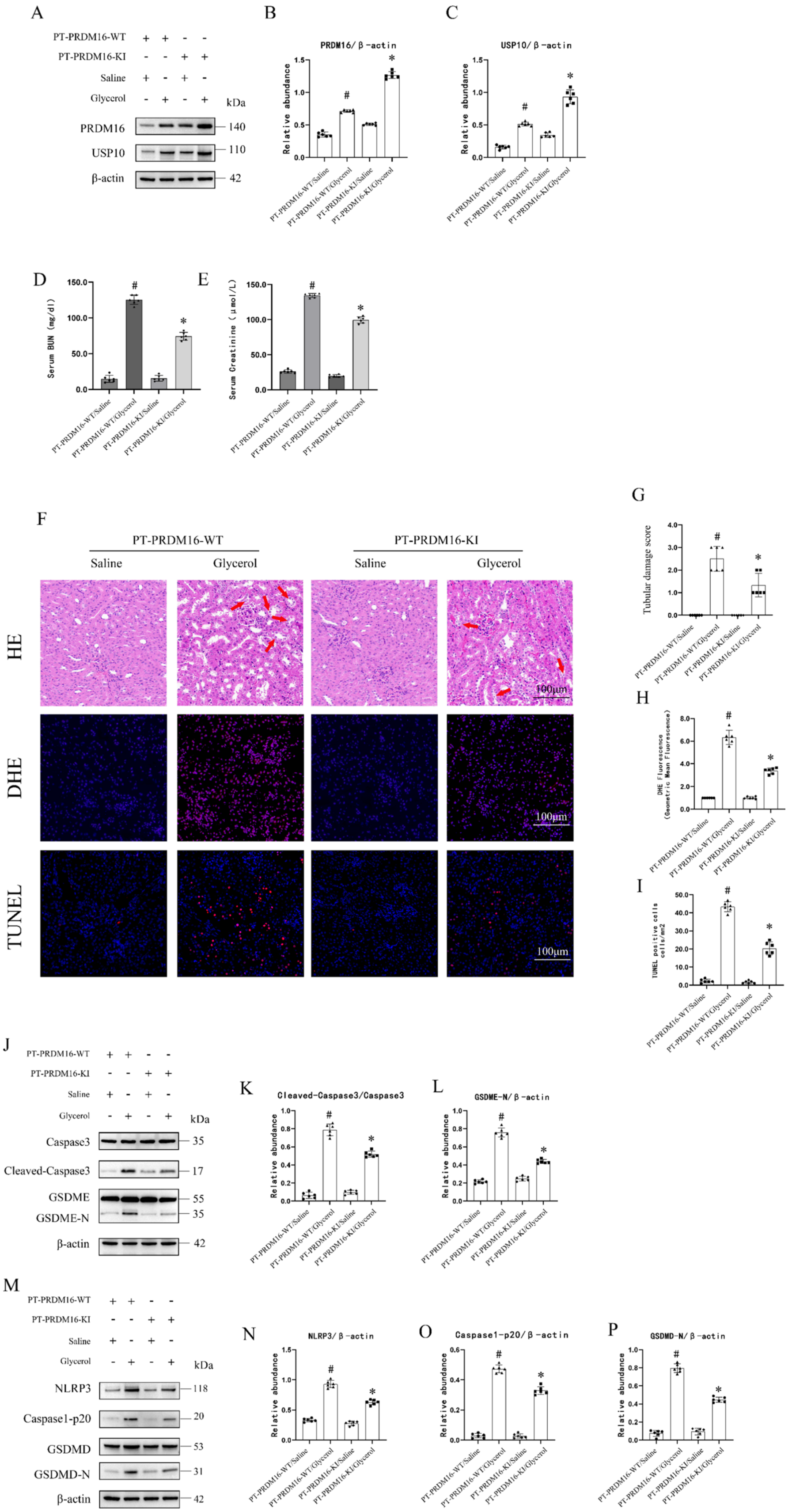

Fig. 10 Renal injury and pyroptosis is alleviated in PT-PRDM16-KI RM-AKI mice. Wild-type mice and PT-PRDM16-KI mice were injected with 50% glycerol to establish rhabdomyolysis-associated acute kidney injury (RM-AKI) model, mice were sacrificed at 24 h. **A** The immunoblot analysis of PRDM16, USP10 and β-actin in mouse kidney. **B** and **C**) Quantitative analysis of PRDM16 and USP10 immunoblot band density. **D** The levels of serum BUN in mice. **E** The levels of serum Creatinine in mice. **F** Representative regions of Hematoxylin–eosin staining, Dihydroethidium staining and TUNEL staining of mouse kidney. **G** Tubular damage score of mouse kidney. **H** Quantification of DHE staining. **I** Quantification of TUNEL-positive staining. **J** The immunoblot analysis of Cleaved-Caspase3, Caspase3, GSDME and β-actin in mouse kidney. **K** and **L** Quantification of Cleaved-Caspase3 and GSDME. **M** The immunoblot analysis of NLRP3, Caspase1-p20 and GSDMD in mouse kidney. **N**–**P** The quantification of NLRP3, Caspase1-p20 and GSDMD. Data are presented as means ± SD (n = 6). # indicates significance ($p < 0.05$) versus PT-PRDM16-WT/Saline group. * indicates significance ($p < 0.05$) versus PT-PRDM16-WT/ Glycerol group

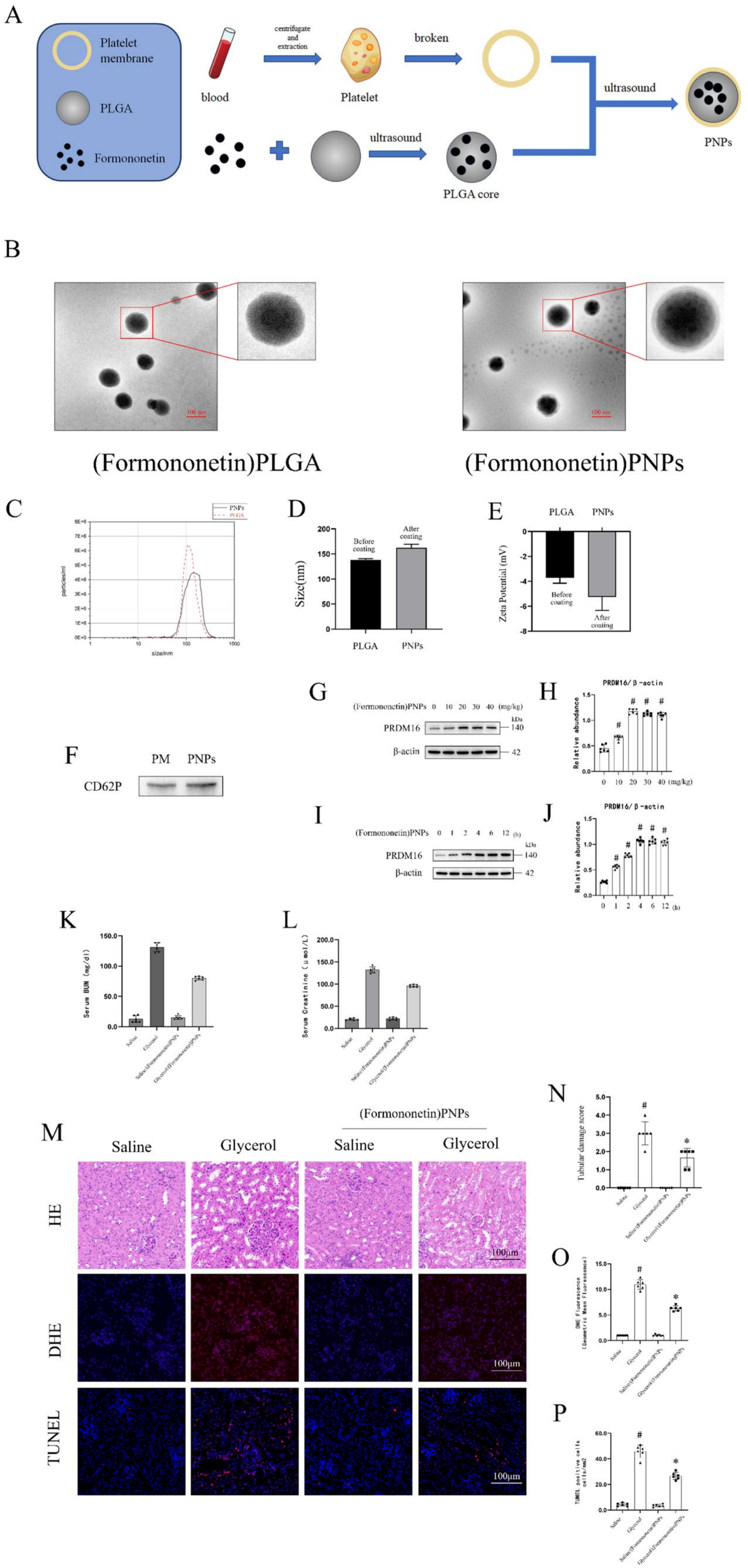

Fig. 11 (Formononetin)PNPs attenuates renal injury in RM-AKI. Rhabdomyolysis-associated acute kidney injury (RM-AKI) mice were injected with (Formononetin)PNPs. **A** Flowchart for the preparation of (Formononetin)PNPs. **B** Representative transmission electron microscopy (TEM) images of (Formononetin)PLGA and (Formononetin)PNPs, Scale bar 100 nm. **C** NTA results for (Formononetin)PLGA and (Formononetin)PNPs. **D** Average particle size of (Formononetin) PNPs. Mean ± SEM. n = 3. **E** Surface Zeta potentials of (Formononetin)PNPs. Mean ± SEM. n = 3. **F** Western blotting to detect the expression of CD62P. **G** and **H** Immunoblot analysis of PRDM16 and β-microtubule proteins in mice injected with different doses (Formononetin)PNPs. **I** and **J** Immunoblot analysis of PRDM16 and β-microtubule proteins at different time points in mice injected with 20 mg/kg dose (Formononetin)PNPs. **K** The levels of serum BUN in mice. **L** The levels of serum Creatinine in mice. **M** Representative regions of Hematoxylin–eosin staining, Dihydroethidium staining and TUNEL staining of mouse kidney. **N** Tubular damage score of mouse kidney. **O** Quantification of DHE staining. **P** Quantification of TUNEL-positive staining. Data are presented as means ± SD (n = 3 for particle size and Surface Zeta potentials; n = 6 for Remaining experiments). # indicates significance ($p < 0.05$) versus (Formononetin) PNPs 0 mg/kg group, (Formononetin) PNPs 0 h group, Saline group. * indicates significance ($p < 0.05$) versus Glycerol group

caused by heavy objects). Glycerol injection is a widely used method for constructing the Rhabdomyolysis-associated Acute Kidney Injury (RM-AKI) model due to its high reproducibility and experimental controllability. In contrast, a major limitation of the non-invasive physical crush injury model is the lack of standardized methodology, factors such as mouse weight, the magnitude of force applied, the duration and area of compression, and post-injury care protocols can vary across studies, which limits the reproducibility of the model conditions and results [56]. Additionally, the experimental equipment required for glycerol injection is more readily available. However, it is important to acknowledge that the glycerol injection model may yield results that differ from those of the physical crush injury model [57], which represents a limitation of this study.

In summary, this research indicates that PRDM16 inhibits pyroptosis and the progression of RM-induced AKI. Mechanistically, PRDM16 promotes USP10 expression, limiting the NLRP3-Caspase1-GSDMD and Caspase3-GSDME axes. The data suggest that PNPs-coated ferromentin represents a promising treatment for RM-induced AKI.

Supplementary Information The online version contains supplementary material available at https://doi.org/10.1007/s00018-025-05666-0.

Acknowledgements The Graphical Abstract was partly generated using Servier Medical Art and brgfx/Freepik, provided by Servier Medical Art, licensed under CC BY 4.0 license. We thank Bullet Editor Limited for the linguistic editing and proofreading of the manuscript.

Author contributions Dongshan Zhang: Methodology, Writing—original draft, Writing—review & editing, Project administration, Supervision, Funding acquisition, Conceptualization. Bocheng Han: Investigation, Writing—original draft, Conceptualization, Software, Methodology, Formal analysis, Visualization, Data curation. Qiang Zheng: Methodology, Project administration, Validation, resources. Huiling Li: Funding acquisition, Project administration. Yongjun Wang: Funding acquisition, Project administration. All authors reviewed the manuscript.

Funding National Natural Science Foundation of China, 82370703, Dongshan Zhang, 82171088, Huiling Li, Natural Science Foundation of Hunan Province, 2023JJ30787, Yongjun Wang.

Data availability Primary data will be available from the authors upon request.

Declarations

Conflict of interests The authors declare no competing interests.

Ethical approval All animal experiments were executed per the protocols set by the Animal Care Ethics Committee of the Second Xiangya Hospital of Central South University (No. 2018065).

Consent to participate Not applicable.

Consent to publish Not applicable.

References

1. Bosch X, Poch E, Grau JM (2009) Rhabdomyolysis and acute kidney injury. N Engl J Med 361(1):62–72
2. Messerer DAC et al (2021) Immunopathophysiology of trauma-related acute kidney injury. Nat Rev Nephrol 17(2):91–111
3. Matsushita K et al (2021) Cilastatin ameliorates rhabdomyolysis-induced AKI in Mice. J Am Soc Nephrol 32(10):2579–2594
4. Lu Y, Neyra JA (2024) how I treat rhabdomyolysis-induced AKI? Clin J Am Soc Nephrol 19(3):385–387
5. Candela N et al (2020) Short- and long-term renal outcomes following severe rhabdomyolysis: a French multicenter retrospective study of 387 patients. Ann Intensive Care 10(1):27
6. Belliere J et al (2015) Specific macrophage subtypes influence the progression of rhabdomyolysis-induced kidney injury. J Am Soc Nephrol 26(6):1363–1377
7. Stewart IJ et al (2015) Retrospective analysis of long-term outcomes after combat injury: a hidden cost of War. Circulation 132(22):2126–2133
8. Liu J et al (2023) Molecular mechanisms of ferroptosis and their involvement in acute kidney injury. J Inflamm Res 16:4941–4951
9. Zhu H et al (2023) Targeting labile iron-mediated ferroptosis provides a potential therapeutic strategy for rhabdomyolysis-induced acute kidney injury. ACS Chem Biol 18(6):1294–1304
10. Chen L, Luo S, Tan H (2024) Penehyclidine hydrochloride improves rhabdomyolysis-mediated acute kidney injury by inhibiting ferroptosis through the HIF-1alpha/MT1G axis. Nephron 148(5):333–344
11. Cen J et al (2024) Synthesis and structure-activity optimization of hydroxypyridinones against rhabdomyolysis-induced acute kidney injury. Eur J Med Chem 263:115933
12. Li N et al (2022) Pathway network of pyroptosis and its potential inhibitors in acute kidney injury. Pharmacol Res 175:106033
13. Al-Kharashi L et al (2023) Pentoxifylline and thiamine ameliorate rhabdomyolysis-induced acute kidney injury in rats via suppressing TLR4/NF-kappaB and NLRP-3/caspase-1/gasdermin mediated-pyroptosis. Toxicol Appl Pharmacol 461:116387
14. Baatarjav C et al (2022) dsDNA-induced AIM2 pyroptosis halts aberrant inflammation during rhabdomyolysis-induced acute kidney injury. Cell Death Differ 29(12):2487–2502
15. Li X et al (2024) (2020) Overexpression of PRDM16 attenuates acute kidney injury progression: genetic and pharmacological approaches. MedComm 5(10):737
16. Zheng Q et al (2024) PRDM16 suppresses ferroptosis to protect against sepsis-associated acute kidney injury by targeting the NRF2/GPX4 axis. Redox Biol 78:103417

17. Sinha D et al (2003) Chemical anoxia of tubular cells induces activation of c-Src and its translocation to the zonula adherens. Am J Physiol Renal Physiol 284(3):F488–F497
18. Xu F et al (2024) Discovery of PRDM16-mediated TRPA1 induction as the mechanism for low tubulo-interstitial fibrosis in diabetic kidney disease. Adv Sci (Weinh) 11(7):e2306704
19. Sun T et al (2021) MBD2 mediates renal cell apoptosis via activation of Tox4 during rhabdomyolysis-induced acute kidney injury. J Cell Mol Med 25(10):4562–4571
20. Okubo K et al (2018) Macrophage extracellular trap formation promoted by platelet activation is a key mediator of rhabdomyolysis-induced acute kidney injury. Nat Med 24(2):232–238
21. Stine RR et al (2019) PRDM16 maintains homeostasis of the intestinal epithelium by controlling region-specific metabolism. Cell Stem Cell 25(6):830–845
22. Robinson JT et al (2023) igvjs: an embeddable JavaScript implementation of the Integrative Genomics Viewer (IGV). Bioinformatics 39(1):830
23. Kulakovskiy IV et al (2018) HOCOMOCO: towards a complete collection of transcription factor binding models for human and mouse via large-scale ChIP-Seq analysis. Nucleic Acids Res 46(D1):D252–D259
24. Maekawa H et al (2019) Mitochondrial damage causes inflammation via cGAS-STING signaling in acute kidney injury. Cell Rep 29(5):1261–1273
25. Li X et al (2020) DsbA-L mediated renal tubulointerstitial fibrosis in UUO mice. Nat Commun 11(1):4467
26. Xu Q et al (2017) MicroRNA-1296 inhibits metastasis and epithelial-mesenchymal transition of hepatocellular carcinoma by targeting SRPK1-mediated PI3K/AKT pathway. Mol Cancer 16(1):103
27. Kim JK et al (2021) Engineered biomimetic platelet membrane-coated nanoparticles block *Staphylococcus aureus* cytotoxicity and protect against lethal systemic infection. Engineering (Beijing) 7(8):1149–1156
28. Yao S et al (2024) Platelet membrane-coated bio-nanoparticles of indocyanine green/elamipretide for NIR diagnosis and antioxidant therapy in acute kidney injury. Acta Biomater 173:482–494
29. Wang Z et al (2023) PRDM16 deficiency in vascular smooth muscle cells aggravates abdominal aortic aneurysm. JCI Insight 8(11):167041
30. Cuevas S, Pelegrin P (2021) Pyroptosis and redox balance in kidney diseases. Antioxid Redox Signal 35(1):40–60
31. Shi J, Gao W, Shao F (2017) Pyroptosis: gasdermin-mediated programmed necrotic cell death. Trends Biochem Sci 42(4):245–254
32. Xia X et al (2019) The role of pyroptosis in cancer: pro-cancer or pro-"host"? Cell Death Dis 10(9):650
33. Li Y et al (2021) GSDME-mediated pyroptosis promotes inflammation and fibrosis in obstructive nephropathy. Cell Death Differ 28(8):2333–2350
34. Bhat AA et al (2023) The pyroptotic role of Caspase-3/GSDME signalling pathway among various cancer: a review. Int J Biol Macromol 242(Pt 2):124832
35. Zhou B et al (2018) Tom20 senses iron-activated ROS signaling to promote melanoma cell pyroptosis. Cell Res 28(12):1171–1185
36. Lin C et al (2024) Modulation of YBX1-mediated PANoptosis inhibition by PPM1B and USP10 confers chemoresistance to oxaliplatin in gastric cancer. Cancer Lett 587:216712
37. Luo P et al (2018) Ubiquitin-specific peptidase 10 (USP10) inhibits hepatic steatosis, insulin resistance, and inflammation through Sirt6. Hepatology 68(5):1786–1803
38. Lian F et al (2024) Ubiquitin-specific peptidase 10 attenuates the ferroptosis to promote thyroid cancer malignancy by facilitating GPX4 via elevating SIRT6. Environ Toxicol 39(3):1129–1139
39. Sango J et al (2022) USP10 inhibits the dopamine-induced reactive oxygen species-dependent apoptosis of neuronal cells by stimulating the antioxidant Nrf2 activity. J Biol Chem 298(1):101448
40. Takahashi M et al (2018) USP10 is a driver of ubiquitinated protein aggregation and aggresome formation to inhibit apoptosis. iScience 9:433–450
41. Takahashi M et al (2013) HTLV-1 Tax oncoprotein stimulates ROS production and apoptosis in T cells by interacting with USP10. Blood 122(5):715–725
42. Gao F et al (2021) USP10 alleviates sepsis-induced acute kidney injury by regulating Sirt6-mediated Nrf2/ARE signaling pathway. J Inflamm (Lond) 18(1):25
43. Wang Q et al (2022) Post-translational control of beige fat biogenesis by PRDM16 stabilization. Nature 609(7925):151–158
44. Ma QX et al (2022) BCAA-BCKA axis regulates WAT browning through acetylation of PRDM16. Nat Metab 4(1):106–122
45. Shen H et al (2022) SOX4 promotes beige adipocyte-mediated adaptive thermogenesis by facilitating PRDM16-PPARgamma complex. Theranostics 12(18):7699–7716
46. Xiong J, Zhao J (2024) Pyroptosis: the determinator of cell death and fate in acute kidney injury. Kidney Dis (Basel) 10(2):118–131
47. Zhao Q et al (2024) FOXQ1, deubiquitinated by USP10, alleviates sepsis-induced acute kidney injury by targeting the CREB5/NF-kappaB signaling axis. Biochim Biophys Acta Mol Basis Dis 1870(7):167331
48. Choi B et al (2020) Recent trends in cell membrane-cloaked nanoparticles for therapeutic applications. Methods 177:2–14
49. Xu L et al (2021) Biomimetic PLGA microbubbles coated with platelet membranes for early detection of myocardial ischaemia-reperfusion injury. Mol Pharm 18(8):2974–2985
50. Dudiki T et al (2023) Mechanism of tumor-platelet communications in cancer. Circ Res 132(11):1447–1461
51. Hu CM et al (2015) Nanoparticle biointerfacing by platelet membrane cloaking. Nature 526(7571):118–121
52. Jiang J et al (2023) Platelet membrane-fused circulating extracellular vesicles protect the heart from ischemia/reperfusion injury. Adv Healthc Mater 12(21):e2300052
53. Li B et al (2021) Platelet-membrane-coated nanoparticles enable vascular disrupting agent combining anti-angiogenic drug for improved tumor vessel impairment. Nano Lett 21(6):2588–2595
54. Hu X et al (2023) Ultrasound-assisted biomimetic nanobubbles for targeted treatment of atherosclerosis. Nanomedicine 51:102682
55. Fei S et al (2024) Platelet membrane biomimetic nanoparticle-targeted delivery of TGF-beta1 siRNA attenuates renal inflammation and fibrosis. Int J Pharm 659:124261
56. Li D et al (2024) Breaking new ground: standardizing rat models for crush syndrome investigations. Shock 61(2):274–282
57. Qiao O et al (2024) Paving the way ahead: protocol optimization of mouse models in crush syndrome related acute kidney injury research. Front Pharmacol 15:1438127

Authors and Affiliations

Bocheng Han[1,2] · Qiang Zheng[2,4] · Huiling Li[3] · Yongjun Wang[1] · Dongshan Zhang[2,5]

✉ Yongjun Wang
wangyongjun@csu.edu.cn

✉ Dongshan Zhang
dongshanzhang@csu.edu.cn

[1] Department of Blood Transfusion, The Second Xiangya Hospital of Central South University, Changsha, Hunan, People's Republic of China

[2] Department of Intensive Care Medicine, The Second Xiangya Hospital of Central South University, Changsha, Hunan, People's Republic of China

[3] Department of Ophthalmology, The Second Xiangya Hospital of Central South University, Hunan, People's Republic of China

[4] Emergency Department, Sichuan Academy of Medical Sciences & Sichuan Provincial People's Hospital, Chengdu, China

[5] Furong Laboratory, Hunan Province, People'S Republic of China, Hunan 410011, People's Republic of China